



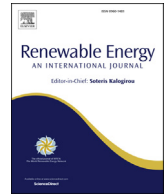
Flow-induced pulsations in Francis turbines during startup - A consequence of an intermittent energy system

Downloaded from: <https://research.chalmers.se>, 2024-03-13 08:05 UTC

Citation for the original published paper (version of record):

Salehi, S., Nilsson, H. (2022). Flow-induced pulsations in Francis turbines during startup - A consequence of an intermittent energy system. *Renewable Energy*, 188: 1166-1183. <http://dx.doi.org/10.1016/j.renene.2022.01.111>

N.B. When citing this work, cite the original published paper.



Flow-induced pulsations in Francis turbines during startup - A consequence of an intermittent energy system

Saeed Salehi^{*}, Håkan Nilsson

Division of Fluid Dynamics, Department of Mechanics and Maritime Sciences, Chalmers University of Technology, Gothenburg, SE, 412 96, Sweden

ARTICLE INFO

Article history:

Received 3 November 2021

Received in revised form

10 January 2022

Accepted 26 January 2022

Available online 7 February 2022

Keywords:

High head Francis turbine

Startup sequence

Flow-induced pulsations

Plunging and rotating modes

Rotating vortex rope (RVR)

OpenFOAM

ABSTRACT

Hydraulic turbines are increasingly responsible for regulating the electric grid, due to the rapid growth of the intermittent renewable energy resources. This involves a large increase in the number of starts and stops, which cause severe flow-induced pulsations and fluctuating forces that deteriorate the machines. Better knowledge of the evolution of the flow in the machines during transients makes it possible to avoid hazardous conditions, plan maintenance intervals, and estimate the costs of this new kind of operation. The present work provides an in-depth and comprehensive numerical study on the flow-induced pulsations and evolution of the flow field in a high-head model Francis turbine during a startup sequence. The flow simulation is carried out using the OpenFOAM open-source CFD code. A thorough frequency analysis is conducted on the fluctuating part of different pressure probes and force components, utilizing Short-Time Fourier Transform (STFT) to extract the evolution of the frequency and amplitude of pulsations. Low-frequency oscillations are detected during the startup, which are induced by the complex flow structure in the draft tube. A decomposition is performed on the draft tube pressure signals, and the variations of the synchronous (plunging) and asynchronous (rotating) modes are studied. The plunging mode is stronger at minimum and deep part load conditions, whereas the rotating mode is dominant during the presence of the Rotating Vortex Rope (RVR) at part load. The velocity field in the draft tube is validated against experimental data, and the complex flow structures formed during the startup procedure are explained using the λ_2 vortex identification method.

© 2022 The Author(s). Published by Elsevier Ltd. This is an open access article under the CC BY license (<http://creativecommons.org/licenses/by/4.0/>).

1. Introduction

The use of renewable electric energy resources has been growing fast to respond to the increasing global electric energy consumption. Nowadays, the inevitable intermittency of electrical energy resources such as solar and wind power is compensated through hydropower systems [1–3]. The hydraulic turbines are not necessarily working at the steady Best Efficiency Point (BEP) condition anymore. They are being used in different transient operating sequences to stabilize the electrical grid, leading to entirely different engineering requirements for such machines.

Transient operations usually produce complex flow structures, such as flow separation, vortices, destructive pressure pulsations, cavitation, etc. Frequent occurrence of such undesirable flow structures could seriously deteriorate the turbine lifetime and

cause fatigue stresses, wear and tear on different components [4]. Currently, Francis turbines may experience over 500 start-stop cycles per year [5], while they are usually designed to tolerate up to 10 cycles [6,7]. Undoubtedly, the accumulated damages from such abundant cycles degrade the machine's performance and may lead to its failure. Hence, it is crucially important to study and provide a profound understanding of the turbine flow field during transient operations such as startup.

Gagnon et al. [8] examined the influence of startup schemes on the fatigue-based life expectancy of a Francis turbine. It was explained that an optimization of the scheme could improve the turbine lifetime. Nicolle et al. [9] assessed the startup operations of a low-head Francis turbine using a reduced CFD model. Two different startup scenarios based on the guide vane opening scheme were investigated. Comparisons were made with limited experimental measurements and a general agreement was achieved.

The impact of the guide vane opening scheme on the startup procedure of a high-head Francis turbine has been experimentally

^{*} Corresponding author.

E-mail addresses: saeed.salehi@chalmers.se (S. Salehi), hakan.nilsson@chalmers.se (H. Nilsson).

assessed by Trivedi et al. [10]. The angular speed of the guide vanes was for one scheme almost twice as for the other scheme. Inappropriate rapid rotation of the guide vanes amplified the unsteadiness and developed undesirable pressure pulsations. Goyal et al. [7] performed an experimental study on the same high-head Francis turbine during startup. The startup sequence was split into two phases, namely, phase I, to synchronize the turbine with the generator, and phase II, to reach the steady-state condition. The second phase was accomplished using three different guide vane opening schemes which ended in Part Load (PL), BEP, and High Load (HL) conditions, respectively. The Rotating Vortex Rope (RVR) frequency was observed in both velocity and pressure data of the first scheme.

More recently, the startup of a prototype Francis turbine was experimentally and numerically investigated [11]. Two guide vane opening schemes, namely, conventional and reduced opening limit schemes were studied and it was shown that the reduced scheme decreased the fatigue damage. The draft tube vortices were shown to have a significantly higher impact on the dynamical stresses compared to the interblade vortices. It was concluded that disturbing the draft tube vortex could alleviate the damaging effects on the runner during startup.

Although the experimental investigations are trustworthy resources to assess the turbine flow field during startup, they are expensive and there are many limitations on accessibility and measured flow details. Numerical studies provide a reliable addition to assess and understand the details of the flow field during turbine startup. The startup is recognized as one of the most harmful operating conditions of hydraulic turbines [8]. Therefore, achieving a profound understanding of the complex flow field of a hydraulic turbine during startup is essential to reduce the damaging effects and improve the life expectancy of these machines.

The present article provides a comprehensive and detailed analysis of the transient flow field and its pulsations during a startup sequence of a Francis turbine. Such in-depth analyses are crucial for a better understanding of the hazardous pulsations to be able to ultimately reduce and avoid them. The simulation is performed utilizing the OpenFOAM open-source CFD code. The variation of the pressure field, velocity field, and forces are carefully assessed. One of the main focuses of the present study is to extract the flow-induced pulsations. No investigations are found in the literature on the draft tube pressure signal decomposition during a startup sequence. In the current study, for the first time, the variation of plunging and rotating modes of the fluctuating pressure during the startup operation is examined. An in-depth explanation of the complex flow structures downstream the runner, which play a crucial role in the generation of the pulsations, is presented. The paper is organized as follows. The investigated test case, including the geometrical and operational details, is introduced in Section 2. The mathematical formulations of the assessed problem are described in Section 3.1, while the details of the numerical framework are described in Section 3. Section 4 provides the numerical results and discussions, and finally, the concluding remarks of the paper are provided in Section 5.

2. Investigated test case

A high-head Francis turbine model is used as the investigated test case. The Francis-99 turbine model, provided by the Francis-99 workshop series [12], is a 1:5.1 scale model of a prototype Francis turbine [13]. The runner consists of 15 full-length and 15 splitter blades. The prototype and model net heads are about $H_{\text{prototype}} \approx 377$ m and $H_{\text{model}} \approx 12$ m, respectively.

Fig. 1a and b show two cross-sections of the Francis-99 model.

The axial and horizontal in-plane velocity components have been experimentally measured at a PIV plane. The PIV plane is shown as a red line and a gray shaded area in the z-normal and y-normal sections, respectively. The velocity measurements are reported on three PIV lines, two horizontal lines (Lines 1 and 2), and one axial line (Line 3). Moreover, the static pressure is reported for three sensor locations, namely, VL2, DT5, and DT6. In the experiments, the draft tube pressure sensors were piezoelectric, and only instantaneous fluctuation of pressure was measured [14]. Two additional numerical probes (RP1 and RP2) are defined in the rotating zone (Runner) to sample the pressure field throughout the sequence. The numerical probes are placed in the middle of one runner passage (in between two neighboring main and splitter blades) at different axial positions.

The current work concerns a startup sequence that commences from the minimum load operating condition. The guide vanes are nearly closed with an opening angle of $\alpha = 0.8^\circ$ and the flow rate is $Q = 0.022$ m³/s. The guide vanes open up, rotating around their axes, and the flow rate increases. The transient sequence ends at the BEP condition in which $\alpha = 9.84^\circ$ and $Q = 0.199$ m³/s. The runner rotational speed remains constant at $\omega = 333$ rpm during the entire transient sequence.

3. Computational framework and numerical aspects

The CFD simulation is carried out with OpenFOAM-v1912 [15,16]. The governing equations are discretized using the finite-volume approach on a collocated mesh. The current section briefly describes the governing equations and the employed numerical methods and schemes. More detailed information about the numerical aspects of the performed CFD simulation is provided by Salehi et al. [17], who used the same approach for a shutdown sequence of the same case.

3.1. Mathematical formulation

A transient incompressible turbulent flow can be modelled by the Unsteady Reynolds-Averaged Navier-Stokes (URANS) equations, given by

$$\frac{\partial U_j}{\partial x_j} = 0, \quad (1)$$

$$\frac{\partial U_i}{\partial t} + \frac{\partial (U_i U_j)}{\partial x_j} = -\frac{1}{\rho} \frac{\partial p}{\partial x_i} + \frac{\partial}{\partial x_j} \left(\nu \frac{\partial U_i}{\partial x_j} - \overline{u_i u_j} \right), \quad (2)$$

where $-\rho \overline{u_i u_j}$ represents the unknown Reynolds stress tensor. The Shear Stress Transport (SST) based Scale-Adaptive Simulation URANS model (i.e., SST-SAS) [18,19] is here employed for the calculation of the Reynolds stress tensor. SST-SAS is a turbulence-resolving URANS model, used for simulations of industrial transient flows. Its formulation decreases the local eddy viscosity to resolve the turbulent spectrum and break-up of large eddies, providing LES-like solutions. Several research studies verified the performance of the SST-SAS model in the simulation of hydraulic machinery flows [11,20–25].

3.2. Discretization schemes

The second-order backward implicit scheme is employed for the discretization of the temporal derivative terms. The time step of the simulation is chosen as $\Delta t = 1.25 \times 10^{-4}$ s, corresponding to runner and guide vane rotations of 0.25° and $1.625 \times 10^{-4}^\circ$ in each time step. The average and maximum CFL numbers at the highest flow

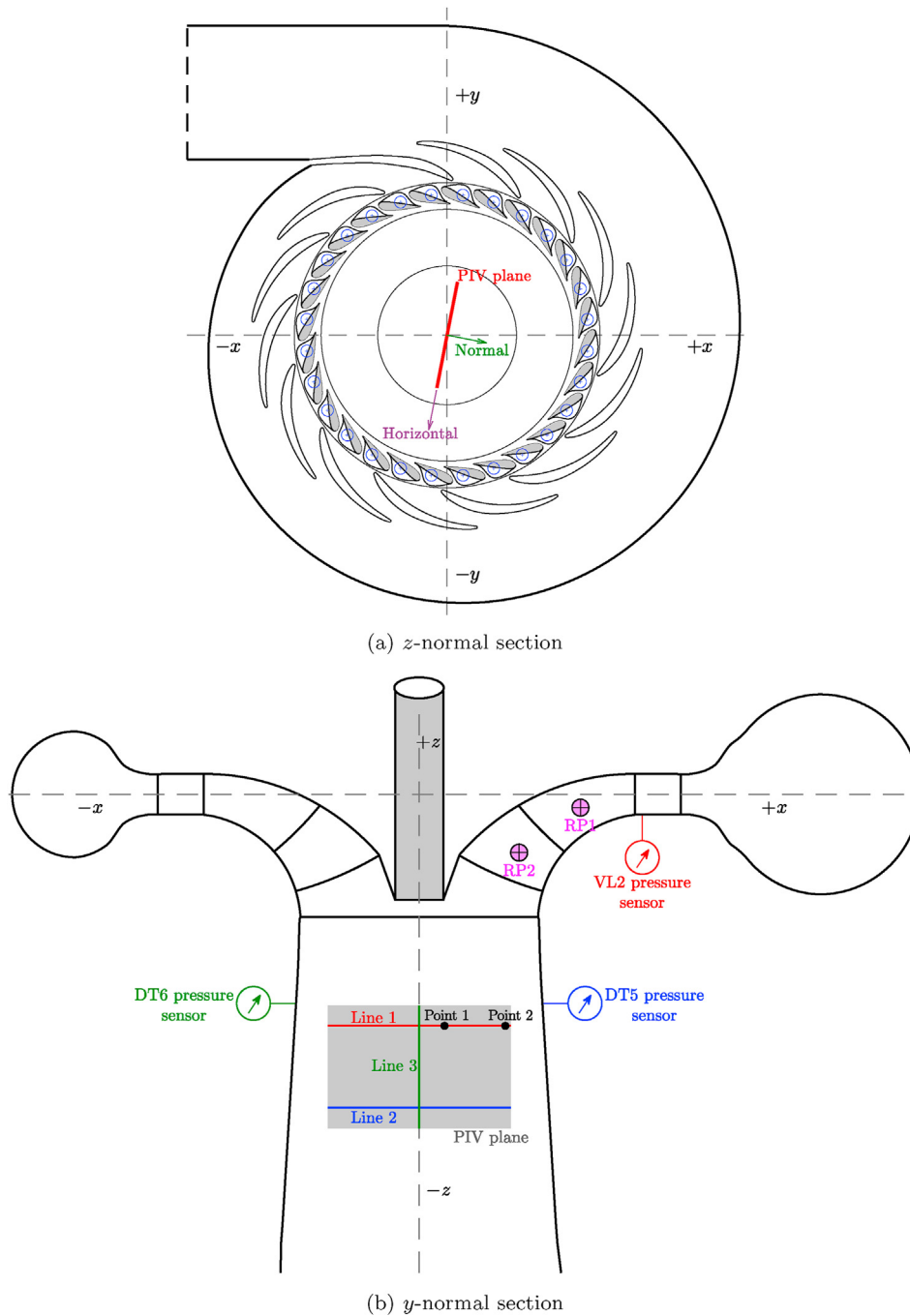


Fig. 1. Two sections of the Francis-99 model, showing PIV plane, velocity lines, pressure sensors.

rate (BEP) are 0.025 and 55. It should be noted that the CFL number is less than 2 for 99.4% of the cells.

The convective terms in the momentum equation are discretized using the Linear-Upwind Stabilised Transport (LUST) scheme [26], which blends the central and second-order upwind schemes with a blending factor of 0.75. In other words, the face values are calculated blending 75% second-order central and 25% second-order upwind schemes, balancing accuracy and numerical stability. The second-order upwind scheme approximates other convective terms (i.e. in k and ω equations).

The Laplacian terms in the transport equations are estimated using the second-order central scheme. An explicit non-orthogonal correction due to the high skewness of the cells at some locations is

inevitable because of the complex geometry.

3.3. Pressure-velocity coupling

The PIMPLE pressure correction algorithm is employed for the pressure-velocity coupling. It combines two pressure correction algorithms, namely, SIMPLE [27] and PISO [28] as outer and inner correction loops, respectively. A maximum of 10 outer correction loops is performed in each time step, controlled by a residual criterion. At most time steps the flow solution is converged after four outer correction loops. Each outer loop conducts two inner correction loops. After each inner loop, one additional non-orthogonal correction loop is performed to assure convergence of

explicit terms. It has been shown that the OpenFOAM implementation of the pressure correction algorithm is in line with the Rhie-Chow interpolation technique [29,30].

3.4. Boundary conditions

The guide vanes open up by rotating with a constant rotational speed of $1.3^\circ/\text{s}$. The time-variation of the guide vane opening angle is plotted in Fig. 2a. As seen in the figure, a smooth transition is implemented at the start and stop of the rotation ($t = 2$ and $t = 9$ s) to minimize the numerical instability caused by the sudden movement of the guide vanes. The total time of the sequence, $t = 12$ s, corresponds to 66.52 runner revolutions.

The guide vane movement is imposed through an ad-hoc developed boundary condition that requires the guide vane rotational speed as input. Therefore, the rotational speed ω of the guide vanes is shown in Fig. 2b.

It is assumed that the inlet volume flow rate of the turbine varies linearly with respect to the guide vanes angle. This assumption is according to the Francis-99 workshop series recommendation due to inaccurate measurements of the flow rate during transient operation [12]. Hence, a time-varying spatially uniform velocity, according to the flow rate, is imposed at the inlet of the spiral casing. A fixed turbulence intensity ($I = 7\%$) and viscosity ratio ($\nu_t/\nu = 100$) is considered for the inflow condition. The inlet pressure is extrapolated from the inside domain using a zero-gradient assumption. All quantities at the outlet boundary are computed using the zero-gradient condition, except the pressure which is set by a fixed value.

As previously described, there are four different mesh regions in the simulation (spiral casing, guide vanes, runner, and draft tube). The Cyclic Arbitrary Mesh Interface (cyclicAMI) [31,32] was utilized to transfer the information between the different domains.

In order to reach a statistically stationary state at minimum load condition, the flow is solved for 4 s flow time corresponding to over 22 runner rotations, and then the startup sequence presented in Fig. 2 is initiated.

3.5. Dynamic mesh framework

CFD analysis of the transient operation of Francis turbines includes two types of simultaneous mesh motion, i.e., mesh deformation of the guide vane domain due to the rotation of each guide vane and solid body rotation of the runner domain. Therefore, a Laplacian displacement mesh morphing solver is employed to deform the guide vane domain mesh while the solid-body rotation

function handled the runner rotations. In each time step, the mesh is updated at the beginning of the first PIMPLE outer correction loop. Then, the face fluxes are calculated based on the face swept volumes and relative fluid velocity [33,34].

The mesh morphing is governed by a Laplace equation, given by

$$\nabla \cdot (\Gamma \nabla \delta_{\text{cell}}) = 0, \quad (3)$$

where Γ is the motion diffusivity and δ_{cell} is the displacement vector of the cell centers. The Laplace equation is solved for the cell-centered displacement (δ_{cell}) and then the solution is interpolated to get the point displacements (δ_{points}). Finally, the new point locations (at time $t + \Delta t$) are simply computed as

$$\mathbf{x}_{\text{point}}^{t+\Delta t} = \mathbf{x}_{\text{point}}^t + \delta_{\text{point}}^t. \quad (4)$$

The motion diffusivity (Γ) is obtained using a quadratic inverse distance scheme with respect to the guide vane surfaces.

Severe mesh deformation of the guide vane region due to the large rotation of the guide vanes during the startup sequence could potentially result in low-quality mesh cells and consequently deterioration of convergence and accuracy of the numerical results. Therefore, in this study, the mesh quality parameters were monitored during the mesh deformation. The guide vane region was remeshed two times at guide vane openings of $\alpha = 3.47^\circ$ and $\alpha = 6.85^\circ$ to maintain an acceptable mesh quality. More information on the numerical aspects and mesh deformation, as well as the open-source case and codes of the current study, is provided by Salehi and Nilsson [35], as the same case and codes are employed in the present work.

A block-structured mesh is created for the CFD simulation. The mesh at BEP contains a total of 16 million cells (for more information please see our previous studies [17,35]).

3.6. Parallel processing

The scotch [36] domain decomposition approach is used to split the computation domain and distribute roughly equal loads to the processors while minimizing their interconnections. The job is submitted to a Linux cluster using 320 CPU cores. The full startup sequence consumed a computational cost of 170,000 core hours.

4. Results and discussion

This section presents the results of the transient startup sequence of the Francis-99 model turbine.

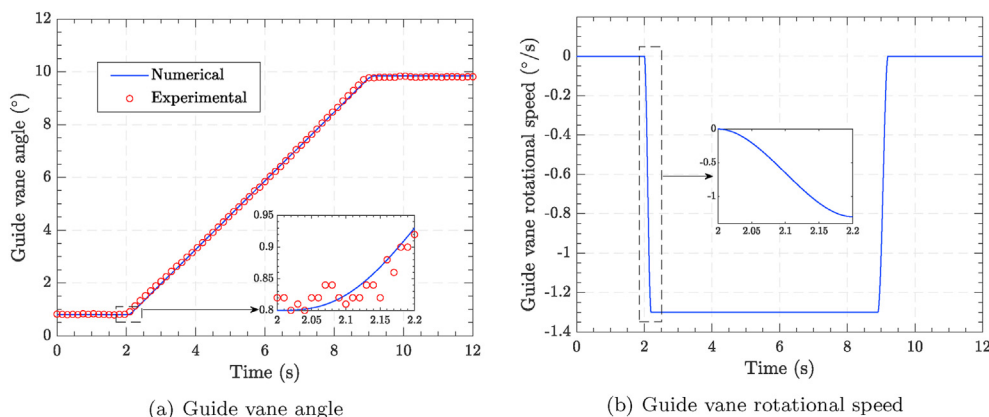


Fig. 2. Variation of (a) guide vane angle and (b) guide vane rotational speed during the startup sequence.

4.1. Pressure fluctuations

As previously described, a number of pressure probes, namely VL2, DT5, DT6, RP1, and RP2, were defined in the computational domain (see Fig. 1), and the variation of the static pressure is recorded throughout the entire startup sequence. The experimental results of the static pressure are available for the VL2 probe, while only the pressure fluctuations were monitored at DT5 and DT6. In transient (time-varying) turbulent flows, as in the current case, the obtained signals (for instance, pressure) consists of two different parts, the mean and fluctuating parts ($p' = p - \bar{p}$). The mean signal changes through time due to the variation of the operating condition. Therefore, in order to extract the fluctuating pressure, the *instantaneous mean* should be calculated. The present study employs the Savitzky-Golay finite impulse response filter [37] for smoothing the obtained signals and calculating instantaneous mean and fluctuations. A variable window size is chosen to capture the fluctuations more accurately. The window is much smaller at the start and end of the transient sequence, where the variation of the pressure level due to the change in operating condition is sharper.

Fig. 3 shows the time-variation of the static pressure, its instantaneous mean, and the fluctuations of the static pressure from its instantaneous mean. In general, the numerical prediction of the VL2 pressure (Fig. 3a) sufficiently matches the experimental data, although with slightly lower values at the BEP condition at the end of the sequence. The maximum relative error, calculated as $|p_{\text{num}} - p_{\text{exp}}|/p_{\text{exp}} \times 100$, is 4.25%. Each plot contains a zoomed view that covers a 90° rotation of the runner in either the stationary minimum load or BEP condition. The VL2 zoomed views show clear

smooth pressure pulsations due to the Rotor-Stator Interaction (RSI) in the vaneless space (between the runner blades and the guide vanes). Since the runner consists of 30 full and splitter blades, 7.5 pressure pulsations can be seen in these zoomed views. The vaneless space static pressure fluctuates around a nearly constant mean pressure at the minimum load condition. Some low-frequency oscillations are also visible at the minimum load condition in the VL2 pressure, which could be due to large unsteady flow structures in the massively separated flow in the draft tube. When the startup sequence commences at $t = 2$ s, the guide vanes start opening up, and consequently, the pressure increases with the turbine flow rate growth. The rate of the pressure increment is initially higher and then it reduces and reaches a constant level until the end of the sequence. The numerical results suggest an overall pressure rise from 160 kPa (at minimum load) to 174 kPa (at BEP). The numerical results reach a stationary condition at $t = 9$ s when the sequence finishes. In contrast, the experimental pressure results show that the flow still needs some time to reach the steady condition, due to dynamics in the experimental open-loop hydraulic system. Some low-frequency oscillations are also visible in the numerical pressure results after the initiation of the sequence. These oscillations are most likely produced by large flow structures formed in the draft tube in the low load conditions and will be discussed in detail later. One can see such pulsations more apparently in the fluctuating pressure shown in Fig. 3b. Distinct periodic oscillatory patterns are seen between $t = 4.5$ s and $t = 6.5$ s that are probably caused by the formation and diminish of the RVR. The static and fluctuating pressure in one of the draft tube probes (DT6) is also shown in Fig. 3c and d. There is not a clear sign of the RSI fluctuations in the presented zoomed views at BEP. Here again,

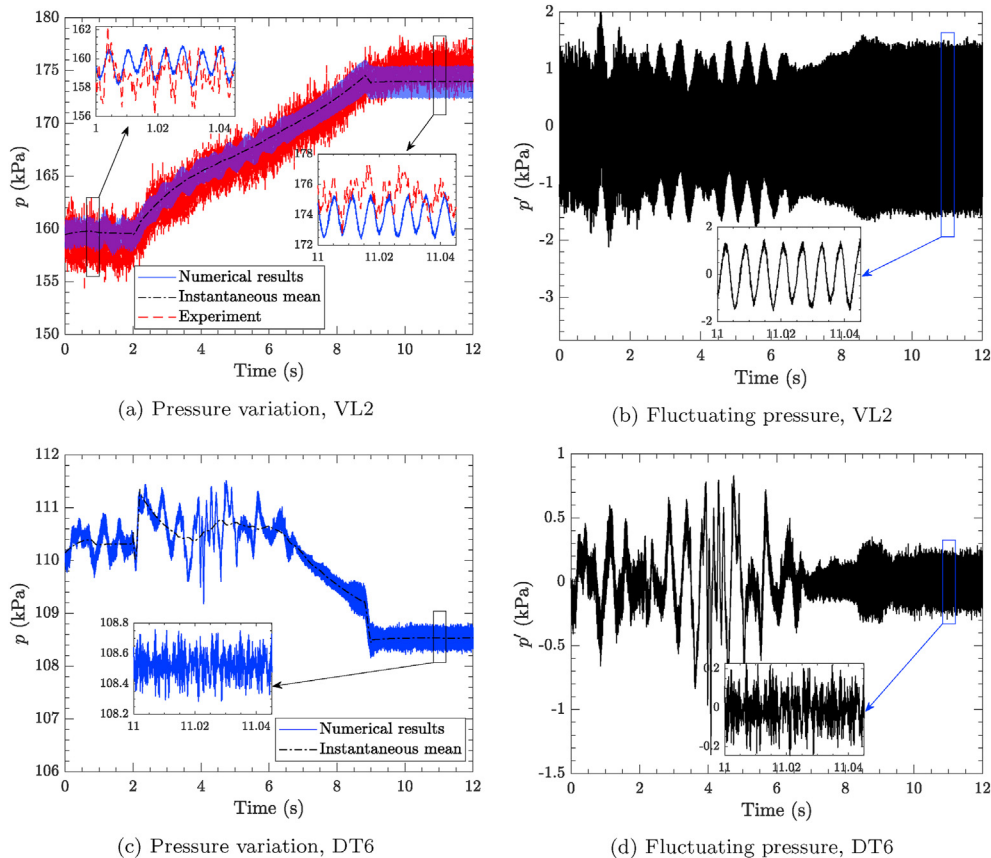


Fig. 3. Time-variation of static pressure (a and c) and its fluctuations from the instantaneous mean (b and d) for two probe locations during startup.

large oscillations are visible in the draft tube pressure at low load conditions.

There are two statistically stationary phases in the whole simulated sequence, namely, the initial minimum load and the final BEP conditions. The Fast Fourier Transform (FFT) analysis technique enables us to identify the excited frequencies and their amplitude of the obtained signals. Therefore, FFT was applied on the fluctuating part of the VL2 and DT6 pressures at both stationary conditions, and the results are plotted in Fig. 4. It should be noted that in the present study, all the frequencies are normalized by the runner rotational frequency $f_n = 5.543$ Hz. The runner blade passing frequency $f_b = 30f_n$ (15 full-length blades and 15 splitter blades) is the dominant frequency in the VL2 probe. The amplitude of f_b is much larger at BEP compared to the minimum load condition. Peaks are visible at the harmonics of the runner passing frequency ($15f_n$ and $60f_n$). A low frequency of approximately $0.3f_n$ is also excited at the minimum load condition of the VL2 pressure, which could be explained by the large separated flow region in the draft tube at such conditions. The draft tube fluctuating pressure (DT6) seems to be most excited at the above-mentioned low frequency. A moderate peak can also be seen at the frequency of $15f_n$, corresponding to the full-length blade passing frequency, as only full-length blades are elongated to the draft tube. In other words, the DT6 draft tube probe can sense the rotation of the full-length blades much more than the splitters.

Due to the time-varying nature of the obtained signals in transient sequences, such as turbine startup, both the excited frequencies and their amplitudes change throughout the sequence. Hence, a Short Time Fourier Transform (STFT) analysis is required for time-frequency analysis. STFT divides the full-time domain into small subdomains and performs the Fourier transform on each subdomain. The time-variations of the amplitudes of different frequencies of the VL2 and DT6 fluctuating pressures are illustrated as spectrograms in Fig. 5. The runner blade passing frequency ($f_b = 30f_n$) is the dominant frequency of the vaneless space pressure throughout the whole sequence (Fig. 5a). The harmonic frequencies (i.e., $15f_n$, $45f_n$, $60f_n$, $75f_n$, etc.) are also clearly excited. A wide range of excited stochastic frequencies are visible in the minimum load condition ($t < 2$ s), indicating a complex flow field including large separations and vortex breakup. When the guide vanes start to open up and the flow rate increases, such frequencies diminish slightly after $t = 2$ s. The zoomed view of the VL2 spectrogram suggests the existence of low-frequency high-amplitude oscillations during the transient sequence. The RVR phenomenon is most likely responsible for such types of pulsations. The DT6 spectrogram denotes a deterministic frequency of $15f_n$, corresponding to

the passing of the full-length blades. The RVR low-frequency oscillations are also clearly visible here.

The time-variation of the amplitude of different excited frequencies is extracted from the STFT calculations and presented in Fig. 6. For the VL2 sensor, the runner blade passing frequency ($30f_n$) is dominant throughout the whole sequence. The amplitude is nearly constant and slightly increases when the turbine reaches the BEP condition. The amplitude of the RVR frequency ($0.3f_n$) is increased with the initiation of the transient sequence and then decreases as the large RVR structures diminish when the turbine approaches the BEP condition. On the other hand, for the DT6 probe, the amplitude of $0.3f_n$ is dominant in the entire sequence, except for the BEP condition where the large draft tube vortical structures are washed away. A sudden rise and then decrease is observed in the amplitude of $0.3f_n$ in the middle of the sequence due to the formation and collapse of the RVR.

Hydraulic turbine draft tube cones generally experience two different types of pressure pulsations at low load conditions [38,39]. The pressure signals can be decomposed into synchronous and asynchronous modes. The synchronous mode (also known as the plunging mode) is somehow similar to the water hammer pressure waves which travel throughout the whole hydraulic system. The asynchronous mode (rotating mode), produced by the local instabilities such as the RVR, is only active in the cross-sections. The pressure signal decomposition can be performed using the unsteady signals of two different pressure probes which are positioned at the opposite sides of the draft tube cone with the same height, through

$$p_{\text{sync}} = \frac{p_1 + p_2}{2} \quad (\text{Synchronous component or plunging mode}),$$

$$p_{\text{async}} = \frac{p_1 - p_2}{2} \quad (\text{Asynchronous component or rotating mode}). \quad (5)$$

A few researchers have studied the draft tube pressure signal decomposition to identify the appearance of plunging and rotating modes at low load conditions of hydraulic turbines (e.g., Refs. [38–42]). However, no investigation can be found in the literature on the decomposition of plunging and rotating modes of a hydraulic draft tube during a startup sequence. Extracting such modes from pressure signals can be particularly helpful for explaining the appearance and collapse of the RVR in transient sequences like shutdown and startup.

In the present test case, the DT5 and DT6 sensors are placed on opposite sides (180° apart) of the conical part of the draft tube and could be used for signal decomposition. First, the synchronous and

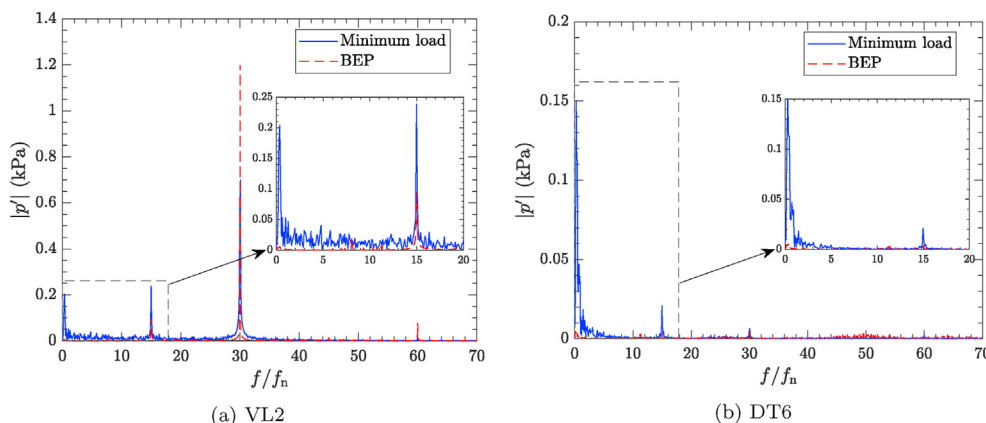


Fig. 4. Fast Fourier Transform of the fluctuating pressure in the stationary conditions at the beginning and end of the sequence (minimum load and BEP).

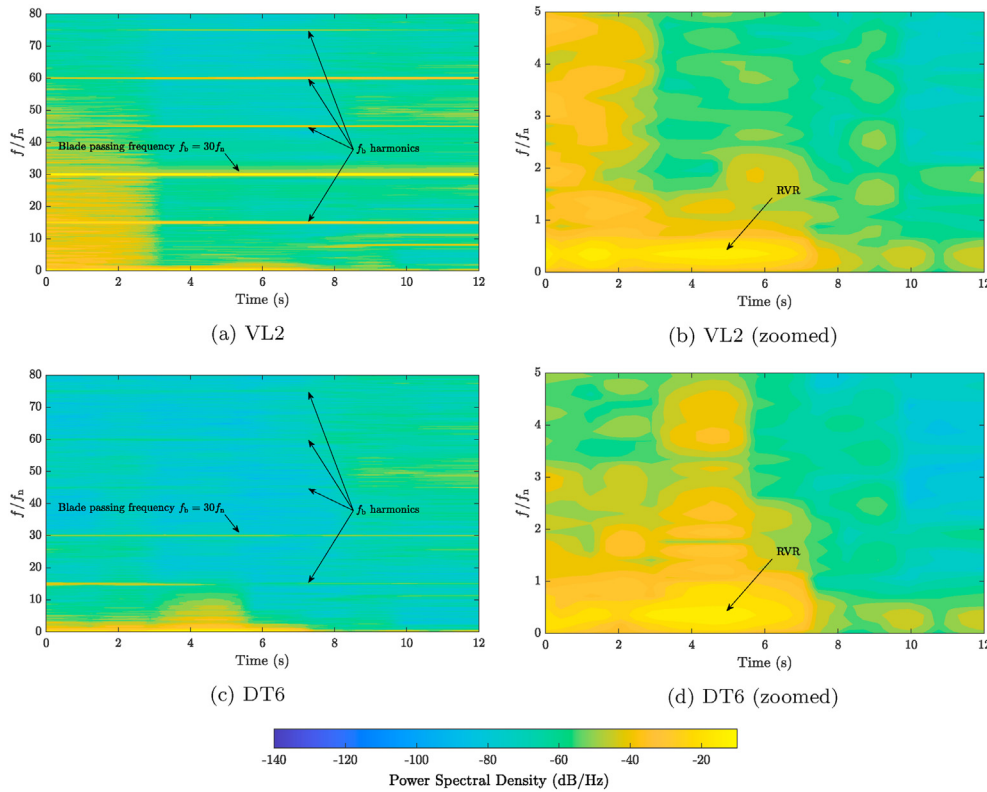


Fig. 5. Spectrogram of fluctuating pressure signal throughout startup sequence.

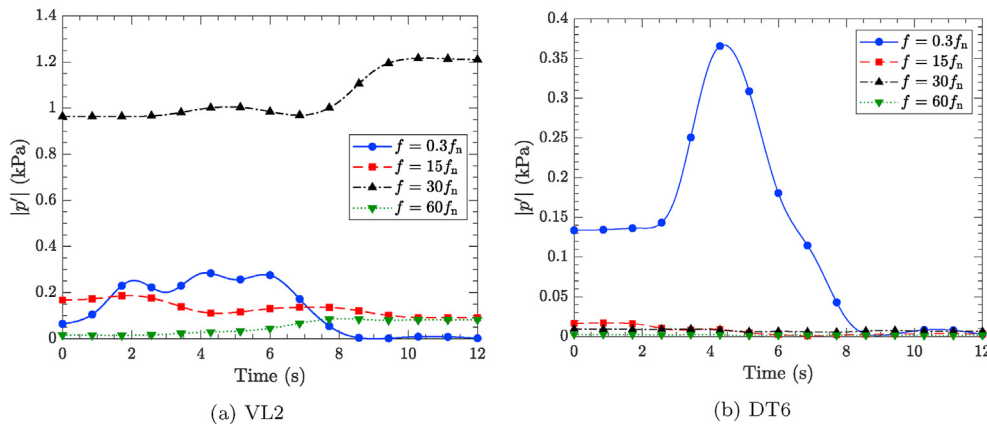
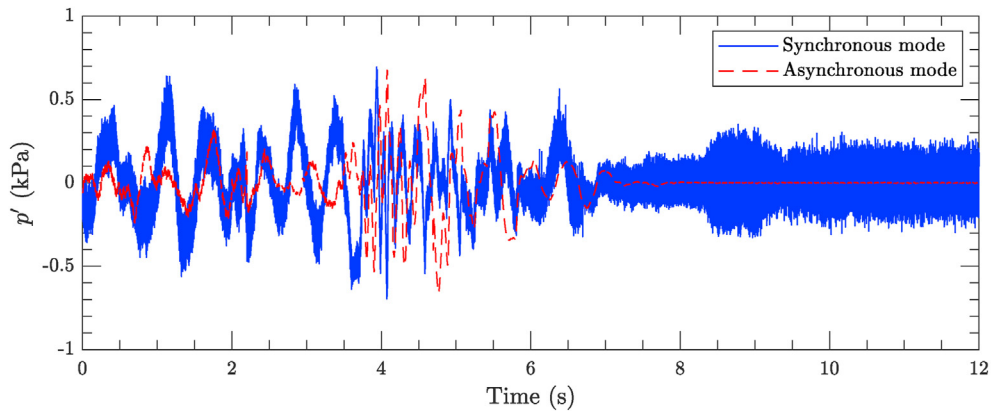


Fig. 6. Variation of fluctuating pressure amplitude over time.

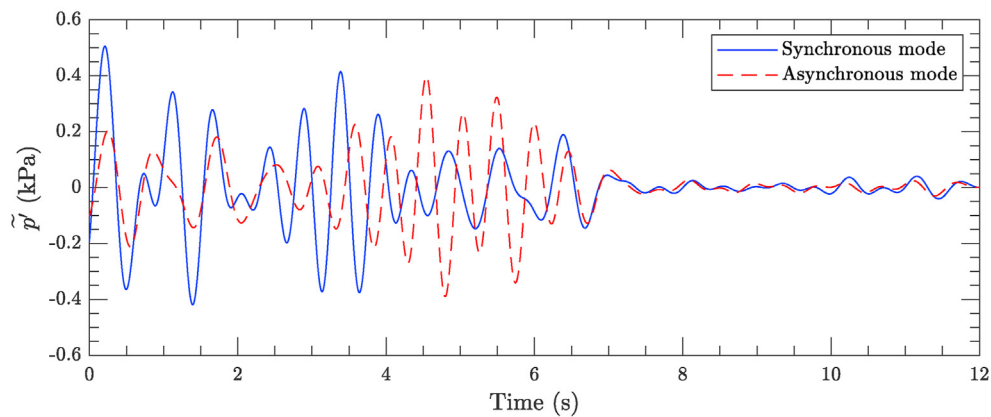
asynchronous modes of the draft tube pressure are computed by inserting DT5 and DT6 pressure signals into Eq. (5) and then the fluctuating parts of each mode are extracted. Fig. 7a presents the time-variation of the fluctuating part of both modes of the draft tube pressure. The high-frequency pressure fluctuations are mostly captured by the synchronous mode. In other words, such fluctuations are in-phase for both probes and are sensed by DT5 and DT6 probes at the same time. Low-frequency oscillations are seen in both synchronous and asynchronous modes at minimum load conditions which decreases when the turbine approaches the BEP condition, indicating that complex flow structures formed at deep part load conditions have strong plunging effects. On the other hand, the asynchronous mode does not show any clear sign of high-frequency fluctuations, and only low-frequency pulsations are

observed. The sudden rise of rotating mode after $t = 4$ s could be a sign of the formation of rotating vortical structures (i.e., RVR) which decays with further increasing turbine load after $t = 6$ s. After $t > 7$ s the turbine approaches the BEP condition and the large vortical flow structures inside the draft tube cone vanish, the pressure fluctuations predominantly contribute to the synchronous mode, and the asynchronous mode is rather negligible at the design condition.

In order to better understand the formation and collapse of the RVR and its impact on the decomposed pressure modes, a bandpass filter with a narrow frequency range of $0.1f_n$, centered at the fundamental frequency of RVR ($0.3f_n$), was applied to the decomposed signals to isolate the RVR effects in the plunging and rotating modes. As previously seen in Figs. 4 and 5, the frequency of $0.3f_n$ is



(a) Fluctuating synchronous and asynchronous pressure modes



(b) Bandpass filtered fluctuating plunging and rotating modes signifying plunging and rotating modes of RVR

Fig. 7. Time-variation of fluctuating synchronous and asynchronous pressure modes. (a) Decomposed signal and (b) bandpass filtered signals.

the dominant frequency inside the draft in a wide range of low-load conditions. The filtered signals displayed in Fig. 7b reveal that the plunging effect is mostly the dominant mode at minimum load and deep part load conditions (before $t = 4$ s), suggesting that disintegrated stochastic flow structures at such conditions primarily cause axial pulsations that are sensed throughout the whole system at the same time. Nonetheless, when the startup sequence of the turbine initiates the rotating effects gradually increase in time while the plunging mode weakens. The fact that the rotating mode is dominant between $t = 4.5$ s and $t = 6.5$ s could be a clear sign of the formation and collapse of the RVR. As expected, no large vortical structures should exist at the BEP condition. Therefore, both the plunging and rotating modes decay after $t = 7$ s.

A time-dependent frequency analysis was performed on the decomposed signals and the results are shown as spectrograms in Fig. 8. Here again, synchronous fluctuations are observed at minimum load and deep part load conditions ($t < 4$ s), while asynchronous pressure pulsations can be detected between $t = 4.5$ s and $t = 6.5$ s. More specially, the fundamental frequency of the RVR is much more pronounced in the rotating mode than the plunging mode during the presence of RVR (between $t = 4.5$ s and $t = 6.5$ s), as also pointed out by Goyal et al. [42].

As explained in Section 2, two probes are defined in the rotating domain of the runner, namely, RP1 and RP2 (see Fig. 1b) and their pressure variation throughout the startup sequence is demonstrated in Fig. 9. Predictably, the RP1 pressure is generally higher than that at RP2, as it is closer to the runner inlet. Both pressure

probes exhibit a gradual rise during the transient sequence. The RP1 pressure increases by 13.3 kPa, whereas the RP2 pressure grows by 7.2 kPa. High-frequency RSI fluctuations are visible through the provided zoomed views. Here the probes are rotating with the runner and therefore the pressure is expected to show a peak whenever the probe is passing a guide vane trailing edge. The fluctuating part of the pressure shows stronger high-frequency RSI fluctuations for RP1 as it is closer to the guide vanes. Both probes contain low-frequency oscillations which are slightly amplified between $t = 4.5$ s and $t = 6.5$ s.

Fig. 10 plots the FFT of the fluctuating pressure of the rotating probes at the stationary conditions (minimum load and BEP). As expected, the fluctuations have a dominant frequency at the guide vane passing frequency ($f_{gv} = 28f_n$) which is stronger at BEP. The first harmonic of this frequency ($f_{gv} = 56f_n$) also shows a small peak. Additionally, some low-frequency peaks, due to the formation and breakup of vortical flow structures are detected by the FFT analysis at minimum load conditions. Since the probes are rotating, the runner rotation frequency (f_n) and its first few harmonics ($2f_n$, $3f_n$, $4f_n$, etc.) are also excited at both conditions. An STFT analysis can further explain the variation of the amplitudes of the excited frequency during the transient sequence. Fig. 11 presents rather similar trends for the time-variation of the amplitudes for both rotating probes. The guide vane passing frequency is a deterministic and dominant frequency during the whole sequence. The zoomed views (Fig. 11b and d) denote that at minimum load condition, a vast range of stochastic frequencies is excited which decay after a short while into the

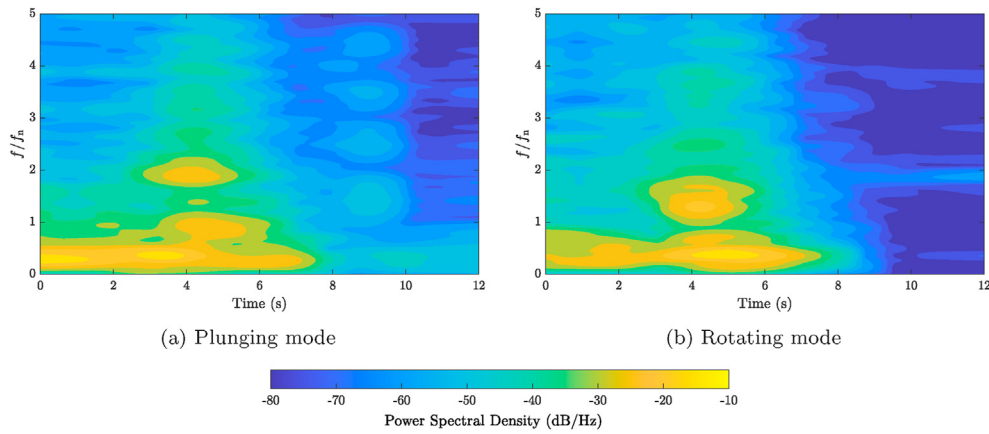


Fig. 8. Spectrogram of fluctuating part of (a) plunging and (b) rotating modes.

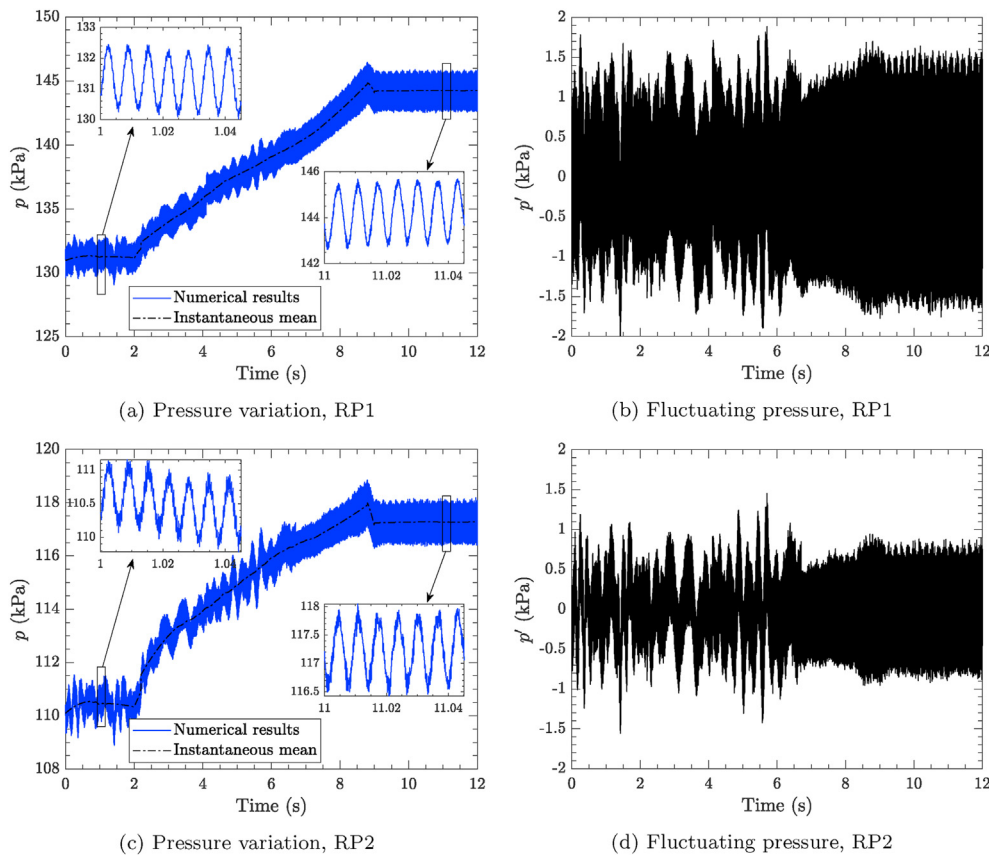


Fig. 9. Time-variation of static pressure (a and c) and its fluctuations from the instantaneous mean (b and d) for two rotating probes (RP1 and RP2) during startup.

transient sequence. Although an excited low frequency is observed during the formation of the RVR (between $t = 4.5$ s and $t = 6.5$ s), the value of that frequency is larger than the RVR fundamental frequency. When the turbine reaches the design condition, the excitation of the runner rotation frequency (f_n) and its harmonics are clearly visible in the zoomed view of both probes.

4.2. Force pulsations

Sharp variations and oscillations of forces and moments exerted on different parts of hydraulic turbines during transient operations could cause serious damages and negatively affect the lifetime of

the turbine. Therefore, performing force analysis during transient sequences like the startup is essential for mitigating such damaging effects. Forces and moments acting on the runner surfaces (i.e., hub, shroud, main blades, and splitters) as well as a single guide vane are monitored during the startup sequence and the results are presented in this section. Although the runner force analysis is performed on the whole runner in the present work, investigating the fluctuating forces on one individual runner blade is suggested for future studies as it could be beneficial for assessing the fatigue effects and lifetime.

Fig. 12 shows the x and z components of the force acting on the runner, as well as the runner torque (z component of moment

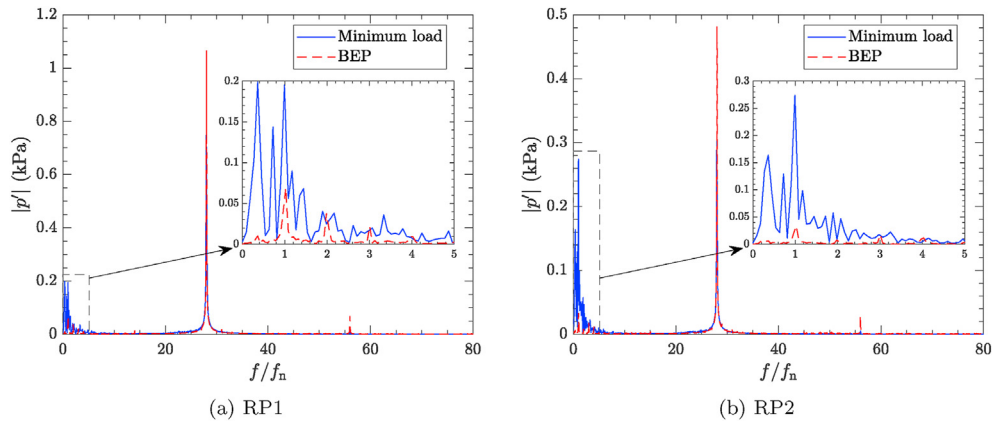


Fig. 10. Fast Fourier Transform of the fluctuating pressure of the rotating probes (RP1 and RP2) during the stationary conditions (minimum load and BEP).

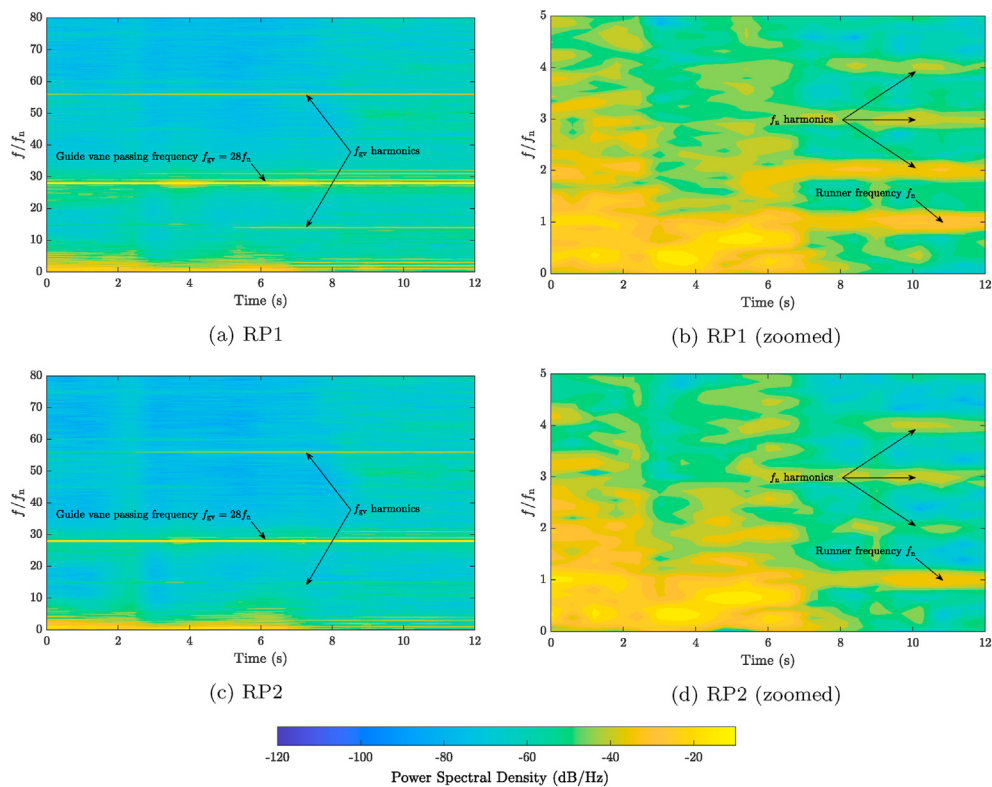


Fig. 11. Spectrogram of fluctuating pressure of rotating probes (RP1 and RP2) throughout startup sequence.

vector). F_x shows strong low-frequency oscillations between $t = 4.5$ s and $t = 6.5$ s, in which the vortex rope is formed and rotates around the turbine axis (Fig. 12a). At the BEP condition, the x -force is fluctuating around a non-zero value, indicating that the flow distribution around the runner is not perfectly axisymmetric. The zoomed view of the fluctuating part of F_x (Fig. 12d) denotes both high and low-frequency oscillations at the BEP condition. The axial force (z -force) is initially oscillating at negative (downward) values at the minimum load condition and shortly after the commencement of the transient sequence it increases and becomes positive (upward) and continues its growth until the BEP condition (Fig. 12b). Comparing the fluctuating parts of F_z and F_x suggests that the low-frequency oscillations during the formation and collapse of the RVR are much weaker for F_z (compared to their corresponding

instantaneous mean). In other words, the RVR mostly affects the horizontal (radial) forces rather than the axial force. This is compatible with the signal decomposition analysis presented in Section 4.1. The axial forces are expected to oscillate with the plunging mode of the RVR, while the radial forces vary with the rotating mode. As elaborated in Fig. 7b, the rotating mode of the RVR is the dominant mode during $t = 4.5$ s and $t = 6.5$ s, and thus the radial force oscillations are greater. The variation of the runner axial torque through time exhibits a smooth linear growth in absolute value of the torque with turbine load increase, from 29.8 N m at minimum load to 630.3 N m at BEP. It is also seen that the fluctuating part of the torque signal is negligible with respect to its instantaneous mean. Fig. 12f reveals that the formation of the RVR barely affects the fluctuating torque and the maximum fluctuating

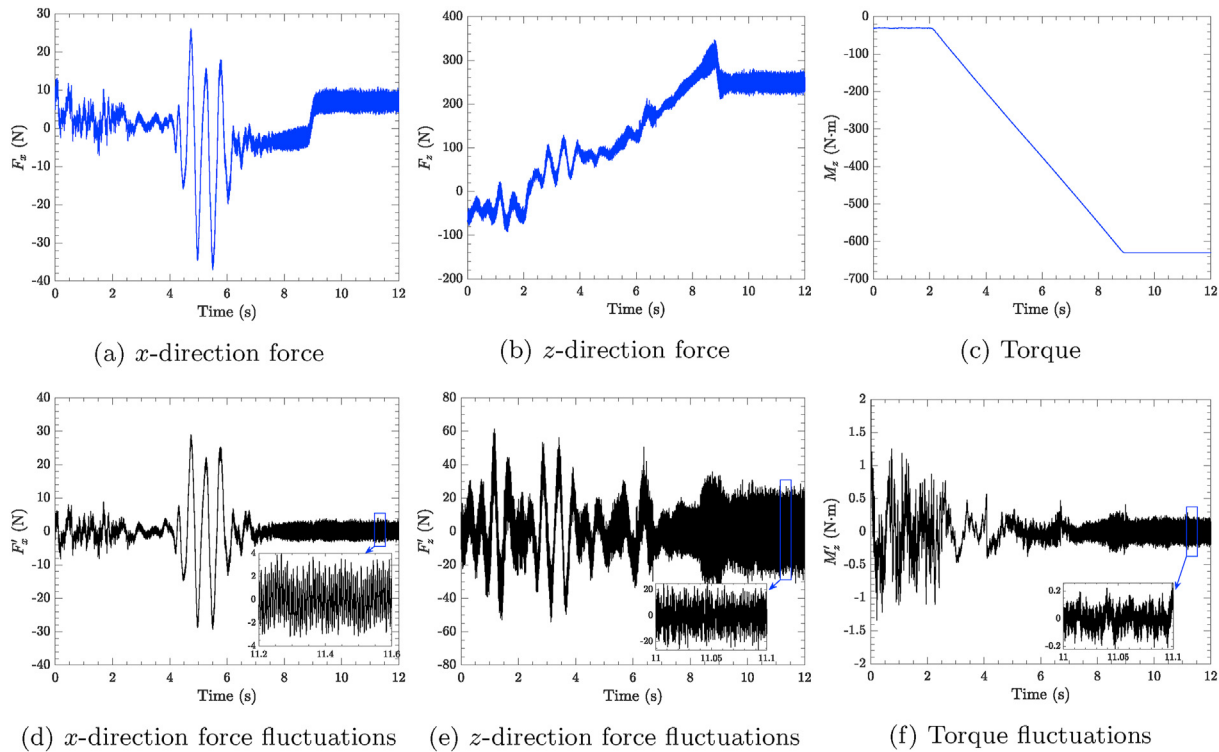


Fig. 12. Variation of components of forces acting on the runner during startup.

torque that occurs at the minimum load condition is less than 1.5 N m.

The spectrograms in Fig. 13 exhibit STFT analysis of the runner forces. The runner blade passing frequency is a deterministic dominant frequency throughout the entire sequence for both the horizontal and axial forces (Fig. 13a and c). The f_b frequency is less isolated in the f_z force and it is more affected by the wide range of stochastic frequencies. The zoomed view of the F_x spectrogram (Fig. 13b) shows mainly stochastic frequencies at minimum load that vanish with the initiation of the sequence. Then the impacts of the RVR on the horizontal forces are clearly seen as low-frequency oscillations. However, the axial forces present a wide range of excited low-frequencies that are not limited to the formation or the collapse of the RVR (Fig. 13d). Here again, we can deduce that complex flow structures at deep part load have strong plunging effects and result in fluctuations of the axial force. The runner rotation frequency (f_n) has an important role in the variation of the horizontal forces at the BEP condition.

To further assess the variation of forces in the Francis-99 startup sequence, the forces and moments acting on a single guide vane are studied. Fig. 14 depicts the time-variation of the radial force and torque (axial moment around the guide vane rotational axis) of the guide vane nearest to the volute tongue. The negative torque acts as to open the guide vane and vice versa. Both plots display smooth variations during the transient sequence with nearly constant ranges of RSI fluctuations, which are larger for the radial force. The F_r is maximum at minimum load and reduces with load increase. More importantly, during the formation and collapse of the RVR (between $t = 4.5$ s and $t = 6.5$ s), F_r oscillates with some low-frequency oscillation but M_z does not show any impact from the RVR. The spectrogram of F'_r , illustrated in Fig. 15, demonstrates a broad span of stochastic frequencies at the minimum load condition. This could be the impact of complex separated flow structures formed behind the trailing edge of the guide vanes at minimum

load condition. Fig. 16 employs an iso-surface of $\lambda_2 = 7500 \text{ s}^{-2}$ to reveal these structures. As expected, the $0.3f_n$ frequency is distinctly evident during the existence of the RVR in Fig. 15.

4.3. Velocity variation

The velocity field is sampled through the entire startup sequence along the three lines shown in Fig. 1 and the numerical results are compared to the experimental data for validation. The variation of the flow field is carefully examined to understand and explain the draft tube flow field during the turbine startup. It should be mentioned that in this work, the horizontal velocity (U) represents the velocity component parallel to Line 1 and 2 (similar but not identical to radial velocity), while the normal velocity (V) is the velocity component normal to the PIV plane (similar but not identical to tangential velocity).

Figs. 17–19 present the time-variation of the numerical velocity components along the three PIV lines (previously shown in Fig. 1). The axial and horizontal velocity components are compared to the experimental measurements. The variable s represents the curve length of each line, which is normalized by its maximum in all plots. The comparison reveals that the numerical axial velocity (W) trend is quite similar to the experiment and thus is adequately well predicted by the simulation. At minimum load condition, the axial velocity direction is upward all over both Lines 1 and 2, varying with low-frequency oscillations. This indicates a massive reversed flow region that covers the entire extent of both lines, while the small mass flow through the draft tube cone passes outside those lines. Then, when the guide vanes start to open up at $t = 2$ s, the reversed flow region gradually gets smaller. The low-frequency oscillations amplify with the establishment of the RVR. After reaching the BEP condition, the reversed flow region completely vanishes and the flow is entirely in the downward direction. At the design condition, the magnitude of W increases with the distance

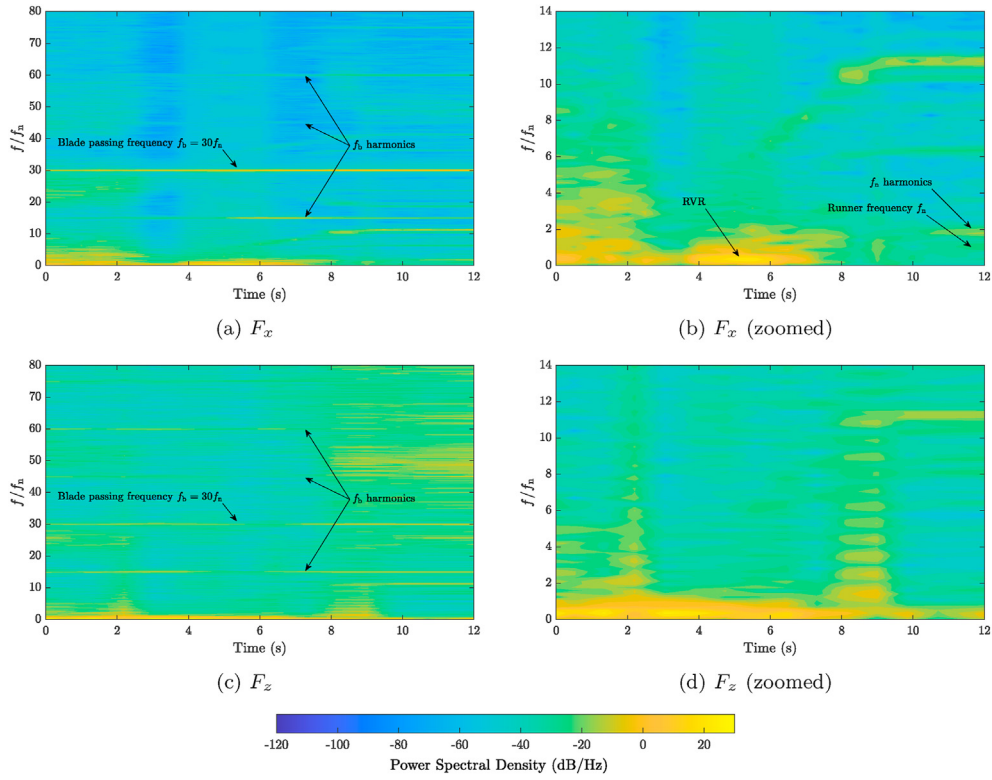


Fig. 13. Spectrogram of fluctuating forces.

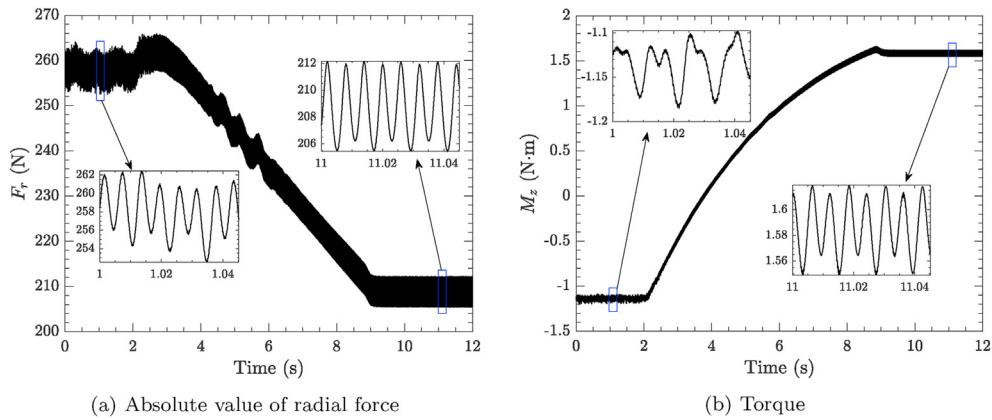


Fig. 14. Variation of radial force and torque acting on one guide vane.

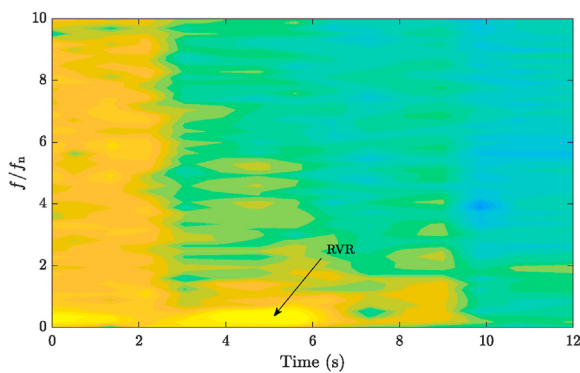


Fig. 15. Spectrogram of fluctuating part of radial force acting on one guide vane.

Fig. 16. Complex vortical structures behind guide vane trailing edges at minimum load condition. Iso-surface of $\lambda_2 = 7500 \text{ s}^{-2}$.

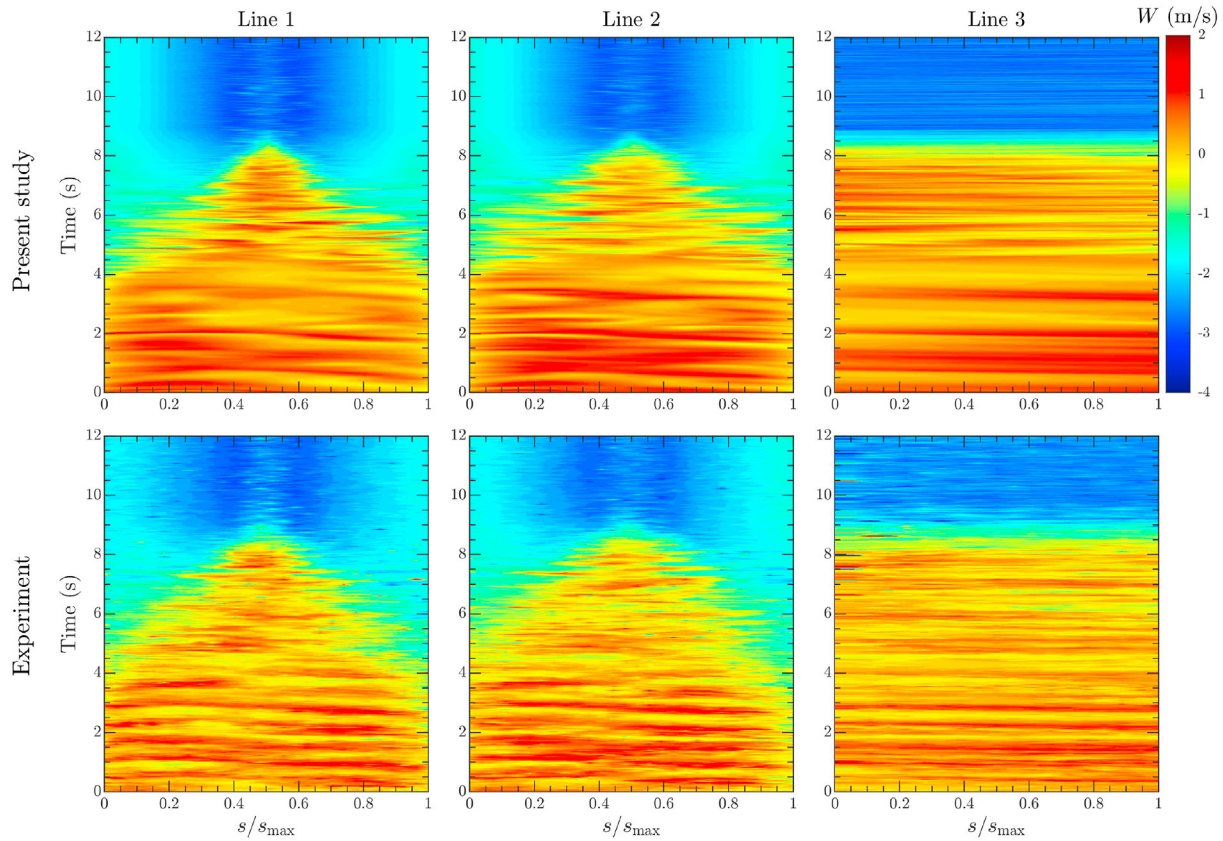


Fig. 17. Time-variation of axial velocity (W) along experimental PIV lines.

to the draft tube walls, whereas it is slightly decreased at the center ($s/s_{\max} = 0.5$) due to the runner cone wake. The fluctuations around the center are induced by the vortex shedding created behind the runner cone. The W contours on Line 3, which is located at the center of the draft tube, denote the existence of the same reversed flow region which is diminished just before reaching the design condition. Both the numerical and experimental data show a rather sharp change in velocity direction around $t = 8$ s.

Fig. 18 indicates that the horizontal velocity mainly fluctuates around zero in both the numerical and experimental data. The fluctuations are initially moderate at minimum load condition and clearly magnify during the formation and collapse of the RVR (between $t = 4.5$ s and $t = 6.5$ s). Then, at the design conditions, both the numerical and experimental results show near-zero U values with small fluctuations.

The normal velocity component (V) was not measured in the experimental study. Therefore, Fig. 19 displays only the numerical results of the time-variation of the normal velocity. A strong swirling flow exists at minimum load condition. The commencement of the startup sequence and load increase temporarily reduces the normal velocity. However, the V component remarkably increases and oscillates with the creation of the RVR. After the collapse of the RVR, the V velocity smoothly reduces. Suddenly before the steady BEP condition, the direction of the V velocity and consequently the swirl orientation changes and a weak counter-rotating flow exists at the design condition.

The time-variation of the velocity field is further assessed using two points, namely Point 1 and 2 (see Fig. 1), in Fig. 20. Both point are placed on Line 1 at radial positions of $R_{\text{Point1}} = 46.5$ mm and $R_{\text{Point2}} = 125.80$ mm, corresponding the normalized curve lengths of $s/s_{\max} = 0.367$ and 0.038 , respectively. Generally, the horizontal velocity oscillates around a near-zero instantaneous mean value.

After $t = 4$ s, large oscillations are visible in the U velocity of Point 2, which is closer to the draft tube wall, whereas Point 1 (close to the center) mainly experience such large fluctuation later (After $t = 6$ s). This implies that the rotating vortical structures (i.e., RVR) form far away from the draft tube center. With load increment, the vortical structures integrate and form a more stable vortex around the center, which results in remarkable fluctuations of U on Point 1 after $t = 6$ s. At the BEP condition, where normally a slender central vortex is observed, Point 1 fluctuates to some extent while Point 2 is quite stable.

The axial velocity initially oscillates around a positive (upward) instantaneous mean at both points in Fig. 20. The turbine load increment gradually increases the magnitude of the axial velocity to a stable point at BEP. The numerical and experimental data show compatible trends. Similar to the U component, the W component at Point 1 does not show large oscillations until $t = 6$ s, while at Point 2 it exhibits extensive fluctuations already after $t = 4$ s.

To examine the swirling flow in the draft tube, the normal velocity (V) is presented in Fig. 20 as well, although no experimental data is available. Positive values of V at Points 1 and 2 indicate a swirling flow in the same direction as the runner rotation, and vice versa.

Water turbines are designed such that a nearly non-swirling flow leaves the runner at BEP. The presence of a weak swirling flow at the design condition could help the flow to stay attached to the draft tube walls. A residual positive (in the same direction of the runner) swirling flow exists at partial load condition, while a higher flow rate than design condition (high load) forms a negative (counter-rotating) residual swirl.

As expected, at minimum load condition a considerable positive tangential component exists, especially on Point 2 which is further from the draft tube center, indicating a large remaining positive

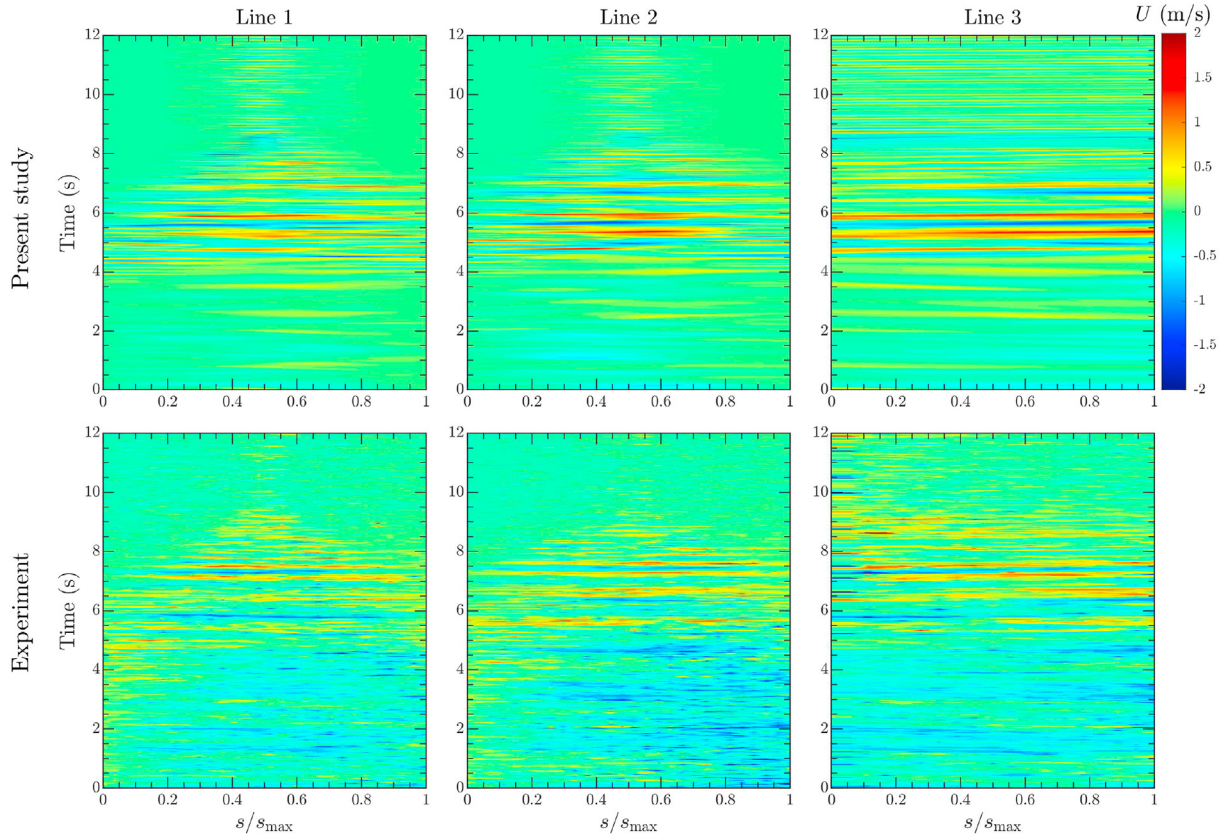


Fig. 18. Time-variation of horizontal velocity (U) along experimental PIV lines.

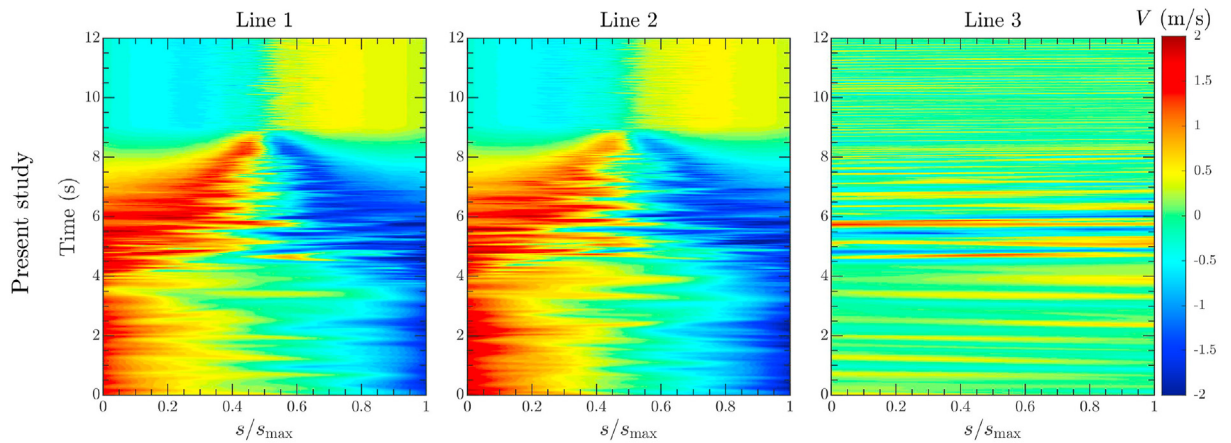


Fig. 19. Time-variation of normal velocity (V) along experimental PIV lines.

swirl in the draft tube. Similar to U and W , the V velocity at Point 2 experiences the large oscillations of the RVR sooner than at Point 1. When the large rotational RVR structures in the draft tube are diminished, the V velocity decreases as the load increases. It settles at an insignificant negative value, indicating a weak counter-rotating swirl at the design condition which could be intentional to keep the flow attached to the draft tube walls.

4.4. Flow structures in the draft tube

The formation and breakup of the vortical flow structures inside the draft tube during the startup sequence is analyzed in this section. Based on a previous study [17], the λ_2 -criterion is employed to

identify and visualize the vortical flow structures. It assumes a vortex to be a region with two negative eigenvalues of the $\mathbf{S}^2 + \mathbf{\Omega}^2$ tensor [43], where \mathbf{S} and $\mathbf{\Omega}$ are the strain and rotation tensors, given by

$$\mathbf{S} = \frac{1}{2}(\nabla \mathbf{U} + \nabla \mathbf{U}^T), \quad \mathbf{\Omega} = \frac{1}{2}(\nabla \mathbf{U} - \nabla \mathbf{U}^T). \quad (6)$$

Therefore, a vortex can be identified as a region with a negative second largest eigenvalue, λ_2 . The OpenFOAM function object `Lambda2` changes the sign of the $\mathbf{S}^2 + \mathbf{\Omega}^2$ tensor eigenvalues, and thus a positive value should be used for the creation of the λ_2 iso-surfaces.

A video is supplied with the article for the readers to see the time-evolution of the vortical structures during the startup operation. Fig. 21 utilizes an iso-surface of $\lambda_2 = 750 \text{ s}^{-2}$ to unveil the evolution of the draft tube vortical structures by 12 snapshots during the turbine startup sequence. The corresponding times (t), guide vane opening angles (α), and the turbine load (normalized flow rate Q/Q_{BEP}) are denoted below each figure. The transient sequence starts from the minimum load condition. At this condition, a massively separated flow field with a significant residual positive swirl exists downstream of the runner (Fig. 21a). As a result, large persistent vortical structures are visible upstream of the draft tube elbow that produces low-frequency pulsations in the flow field and turbine forces. When the transient sequence initiates at $t = 2 \text{ s}$, the guide vanes start to open up and the turbine load increases. Consequently, the growing flow rate washes down the large vortical structures (Fig. 21b and c).

At $t = 4.2 \text{ s}$ (Fig. 21d) the aforementioned large vortices are completely vanished and instead elongated vortical structures are formed downstream the runner. These are formed due to the instability of the shear layer between the swirling downward and separated upward flow regions. The separated region is still quite large and thus the shear layer is close to the draft tube wall. Four distinct draft tube vortices are formed in this region. Continuing the startup sequence, the vortical flow structures develop and expand (Fig. 21e). Thereafter, further opening the guide vanes, the stagnant (reversed flow) region shrinks. Accordingly, the unstable vortical structures gradually integrate and form a large unstable coherent structure that is helically wrapped around the stagnant region (Fig. 21f and g). An integrated rotating vortex rope is clearly distinguishable at time $t = 6.0 \text{ s}$ (Fig. 21g) due to Kelvin–Helmholtz instability of the sharp shear layer. This is in accordance with the results presented in Sections 4.1–4.3, where distinct low-frequency high-amplitude oscillations were observed between $t = 4.5 \text{ s}$ and

$t = 6.5 \text{ s}$.

The additional augmentation of the flow rate decreases the runner residual swirl and squeezes the stagnant region. Inevitably, the integrated central vortex becomes more stable and moves toward the center of the draft tube (Fig. 21h and i). One can see small vortices that rotate around the central axis and merge into a stable slender vortex that is attached to the runner cone (Fig. 21j and k). Finally, the turbine reaches the BEP condition where a small negative (counter-rotating) swirl leaves the runner and forms a stable and nearly stationary vortex at the center of the draft tube.

5. Conclusion

The present paper provides a detailed numerical study on the pulsations originated by the transient flow features during the startup of a high-head model Francis turbine. Our results contribute to a better knowledge of the evolution of the flow in the hydraulic turbines during startup operation that could provide the possibility to avoid harmful conditions and have a better estimate of maintenance intervals and costs.

The high-frequency pulsations generated by the blade passing rotor-stator interaction ($30f_n$) were the dominant excited frequency in the vaneless space throughout the entire startup sequence, while the guide vane passing frequency ($28f_n$) was the dominant mode for the pressure probe inside the runner rotating domain. Low-frequency high-amplitude oscillations were observed in the middle of the sequence, suggesting the formation of the RVR. A signal decomposition of the draft tube pressure indicated that the complex flow structures formed at minimum and deep part load conditions have strong plunging (synchronous) effects. Increasing turbine load gave a sudden rise in rotating (asynchronous) mode during the formation of the RVR.

Low-frequency oscillations of the RVR affect the radial forces

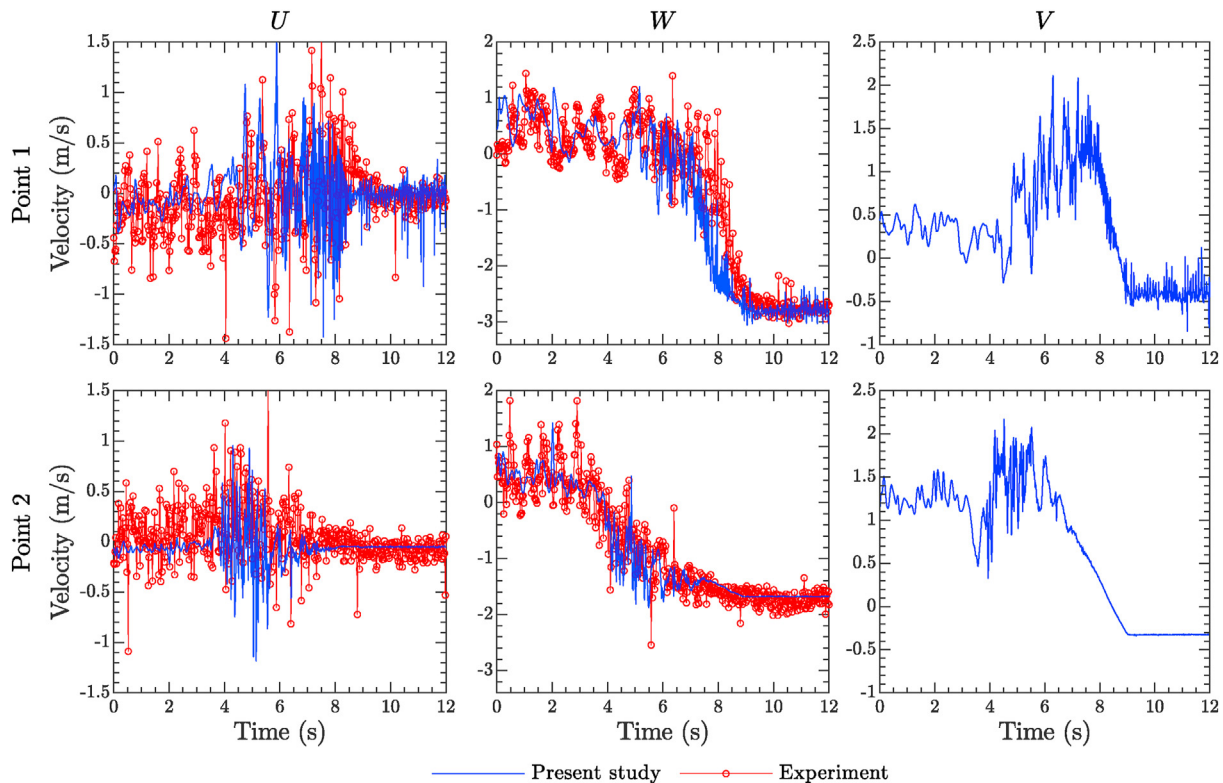


Fig. 20. Time-variation of horizontal (U), axial (W), and normal (V) velocity components on Points 1 and 2 compared to the experimental PIV data.

acting on the runner more than the axial force. The blade passing frequency is less isolated in the axial force compared to the radial component. The axial force is greatly affected by the plunging effects at the minimum load condition and thereby its STFT shows mainly stochastic frequencies. A frequency analysis of the

fluctuating radial force exerted on the guide vanes revealed a broad span of stochastic frequencies at the minimum load condition due to the massively separated flow field behind the nearly closed guide vanes.

The velocity field in the draft tube revealed the presence of a

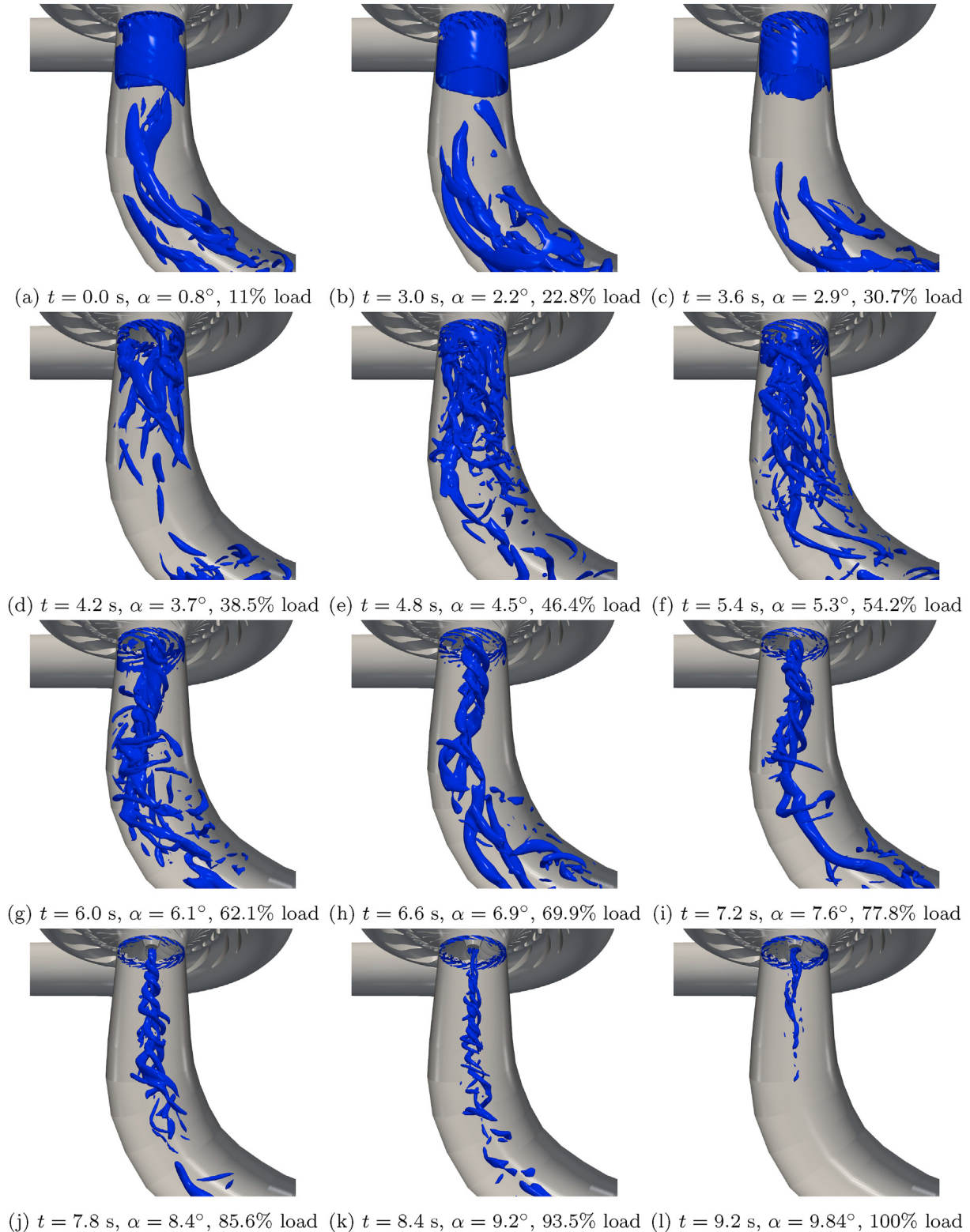


Fig. 21. Illustration of draft tube vortical structures using an iso-surface of $\lambda_2 = 750 \text{ s}^{-2}$ at different times corresponding to different guide vane openings (α).

large quasi-stagnant region with a large positive residual swirl that reduces during the sequence. Large persistent vortical structures were observed inside the draft tube at the minimum load condition. They are responsible for the low-frequency oscillations in such conditions. Gradually increasing the turbine load results in an integration of the unstable vortical structures and the formation of the RVR. At BEP a slender stable vortical structure was observed near the center of the draft tube.

CRedit authorship contribution statement

Saeed Salehi: Conceptualization, Methodology, Software, Investigation, Writing – review & editing. **Håkan Nilsson:** Conceptualization, Supervision, Writing – review & editing, Funding acquisition.

Declaration of competing interest

The authors declare that they have no known competing financial interests or personal relationships that could have appeared to influence the work reported in this paper.

Acknowledgements

The current research was carried out as a part of the “Swedish Hydropower Centre – SVC”. SVC is established by the Swedish Energy Agency, EnergiForsk and Svenska Kraftnät together with Luleå University of Technology, The Royal Institute of Technology, Chalmers University of Technology and Uppsala University, www.svc.nu.

The computations were enabled by resources provided by the Swedish National Infrastructure for Computing (SNIC) at NSC partially funded by the Swedish Research Council through grant agreement no. 2018–05973.

The investigated test case is provided by NTNU – Norwegian University of Science and Technology under the Francis-99 workshop series.

Appendix A. Supplementary data

Supplementary data to this article can be found online at <https://doi.org/10.1016/j.renene.2022.01.111>.

References

- [1] G. Caralis, D. Papantonis, A. Zervos, The role of pumped storage systems towards the large scale wind integration in the Greek power supply system, *Renew. Sustain. Energy Rev.* 16 (5) (2012) 2558–2565, <https://doi.org/10.1016/j.rser.2012.01.068>.
- [2] J. Hell, High flexible hydropower generation concepts for future grids, *J. Phys. Conf.* 813 (2017), 012007, <https://doi.org/10.1088/1742-6596/813/1/012007>.
- [3] R. Goyal, B.K. Gandhi, Review of hydrodynamics instabilities in Francis turbine during off-design and transient operations, *Renew. Energy* 116 (2018) 697–709, <https://doi.org/10.1016/j.renene.2017.10.012>.
- [4] C. Trivedi, B. Gandhi, C.J. Michel, Effect of transients on Francis turbine runner life: a review, *J. Hydraul. Res.* 51 (2) (2013) 121–132, <https://doi.org/10.1080/00221686.2012.732971>.
- [5] C. Deschênes, R. Fraser, J.-P. Fau, New trends in turbine modelling and new ways of partnership, in: *International Conference on Hydraulic Efficiency Measurement—IGHM*, Toronto, Ontario, Canada, July, 2002, pp. 17–19.
- [6] H.-J. Huth, *Fatigue Design of Hydraulic Turbine Runners*, Ph.D. thesis, Norwegian University of Science and Technology (NTNU), 2005.
- [7] R. Goyal, M.J. Cervantes, B.K. Gandhi, Synchronized PIV and pressure measurements on a model Francis turbine during start-up, *J. Hydraul. Res.* 58 (1) (2020) 70–86, <https://doi.org/10.1080/00221686.2018.1555551>.
- [8] M. Gagnon, S.A. Tahan, P. Bocher, D. Thibault, Impact of startup scheme on Francis runner life expectancy, *IOP Conf. Ser. Earth Environ. Sci.* 12 (2010), 012107, <https://doi.org/10.1088/1755-1315/12/1/012107>.
- [9] J. Nicolle, J.F. Morissette, A.M. Giroux, Transient CFD simulation of a Francis turbine startup, *IOP Conf. Ser. Earth Environ. Sci.* 15 (6) (2012), 062014, <https://doi.org/10.1088/1755-1315/15/6/062014>.
- [10] C. Trivedi, M.J. Cervantes, B.K. Gandhi, O.G. Dahlhaug, Experimental investigations of transient pressure variations in a high head model Francis turbine during start-up and shutdown, *J. Hydrodyn. B* 26 (2) (2014) 277–290, [https://doi.org/10.1016/S1001-6058\(14\)60031-7](https://doi.org/10.1016/S1001-6058(14)60031-7).
- [11] J. Unterluggauer, V. Sulzgruber, E. Doujak, C. Bauer, Experimental and numerical study of a prototype Francis turbine startup, *Renew. Energy* 157 (2020) 1212–1221, <https://doi.org/10.1016/j.renene.2020.04.156>.
- [12] Francis-99, <https://www.ntnu.edu/nvks/francis-99>, 2020. (Accessed 28 January 2020).
- [13] C. Trivedi, M.J. Cervantes, B.K. Gandhi, O.G. Dahlhaug, Experimental and numerical studies for a high head Francis turbine at several operating points, *J. Fluid Eng.* 135 (11) (08 2013) 111102, <https://doi.org/10.1115/1.4024805>.
- [14] R. Goyal, *Flow Field in a High Head Francis Turbine Draft Tube during Transient Operations*, Ph.D. thesis, Luleå University of Technology, 2017.
- [15] H.G. Weller, G. Tabor, H. Jasak, C. Fureby, A tensorial approach to computational continuum mechanics using object-oriented techniques, *Comput. Phys.* 12 (6) (1998) 620, <https://doi.org/10.1063/1.168744>.
- [16] OpenCFD, *OpenFOAM – the Open Source CFD Toolbox – User's Guide, Version vol. 2006*, OpenCFD Ltd, 2020.
- [17] S. Salehi, H. Nilsson, E. Lillberg, N. Edh, An in-depth numerical analysis of transient flow field in a Francis turbine during shutdown, *Renew. Energy* 179 (2021) 2322–2347, <https://doi.org/10.1016/j.renene.2021.07.107>.
- [18] F. Menter, Y. Egorov, A scale adaptive simulation model using two-equation models, in: 43rd AIAA Aerospace Sciences Meeting and Exhibit, 2005, p. 1095, <https://doi.org/10.2514/6.2005-1095>.
- [19] Y. Egorov, F. Menter, Development and application of SST-SAS turbulence model in the DESIDER project, in: S.-H. Peng, W. Haase (Eds.), *Advances in Hybrid RANS-LES Modelling*, Springer Berlin Heidelberg, Berlin, Heidelberg, 2008, pp. 261–270.
- [20] T. Krappel, A. Ruprecht, S. Riedelbauch, R. Jester-Zuerker, A. Jung, Investigation of Francis turbine part load instabilities using flow simulations with a hybrid RANS-LES turbulence model, *IOP Conf. Ser. Earth Environ. Sci.* 22 (3) (2014), 032001, <https://doi.org/10.1088/1755-1315/22/3/032001>.
- [21] A. Javadi, H. Nilsson, A comparative study of scale-adaptive and large-eddy simulations of highly swirling turbulent flow through an abrupt expansion, *IOP Conf. Ser. Earth Environ. Sci.* 22 (2) (2014), 022017, <https://doi.org/10.1088/1755-1315/22/2/022017>.
- [22] J. Nicolle, S. Cupillard, Prediction of dynamic blade loading of the Francis-99 turbine, *J. Phys. Conf.* 579 (2015), 012001, <https://doi.org/10.1088/1742-6596/579/1/012001>.
- [23] C. Trivedi, Investigations of compressible turbulent flow in a high-head Francis turbine, *J. Fluid Eng.* 140 (1) (09 2017), 011101, <https://doi.org/10.1115/1.4037500>.
- [24] J. Decaix, V. Hasmatuchi, M. Titzschkau, C. Münch-Alligné, CFD investigation of a high head Francis turbine at speed no-load using advanced URANS models, *Appl. Sci.* 8 (12) (2018) 2505, <https://doi.org/10.3390/app8122505>.
- [25] N. Sotoudeh, R. Maddahian, M.J. Cervantes, Investigation of rotating vortex rope formation during load variation in a Francis turbine draft tube, *Renew. Energy* 151 (2020) 238–254, <https://doi.org/10.1016/j.renene.2019.11.014>.
- [26] H. Weller, Controlling the computational modes of the arbitrarily structured C grid, *Mon. Weather Rev.* 140 (10) (2012) 3220–3234, <https://doi.org/10.1175/MWR-D-11-00221.1>.
- [27] S. Patankar, D. Spalding, A calculation procedure for heat, mass and momentum transfer in three-dimensional parabolic flows, *Int. J. Heat Mass Tran.* 15 (10) (1972) 1787–1806, [https://doi.org/10.1016/0017-9310\(72\)90054-3](https://doi.org/10.1016/0017-9310(72)90054-3).
- [28] R. Issa, Solution of the implicitly discretised fluid flow equations by operator-splitting, *J. Comput. Phys.* 62 (1) (1986) 40–65, [https://doi.org/10.1016/0021-9991\(86\)90099-9](https://doi.org/10.1016/0021-9991(86)90099-9).
- [29] C.M. Rhie, W.L. Chow, Numerical study of the turbulent flow past an airfoil with trailing edge separation, *AIAA J.* 21 (11) (1983) 1525–1532, <https://doi.org/10.2514/3.8284>.
- [30] F.P. Kärrholm, *Numerical Modelling of Diesel Spray Injection, Turbulence Interaction and Combustion*, Ph.D. thesis, Chalmers University of Technology Gothenburg, Sweden, 2008.
- [31] P. Farrell, J. Maddison, Conservative interpolation between volume meshes by local galerkin projection, *Comput. Methods Appl. Mech. Eng.* 200 (1) (2011) 89–100, <https://doi.org/10.1016/j.cma.2010.07.015>.
- [32] H.J. Aguerre, S. Márquez Damián, J.M. Gimenez, N.M. Nigro, Conservative handling of arbitrary non-conformal interfaces using an efficient supermesh, *J. Comput. Phys.* 335 (2017) 21–49, <https://doi.org/10.1016/j.jcp.2017.01.018>.
- [33] H. Jasak, Z. Tukovic, Automatic mesh motion for the unstructured finite volume method, *Trans. FAMENA* 30 (2) (2006) 1–20.
- [34] H. Jasak, Dynamic mesh handling in OpenFOAM, in: 47th AIAA Aerospace Sciences Meeting Including the New Horizons Forum and Aerospace Exposition, 2009, p. 341, <https://doi.org/10.2514/6.2009-341>.
- [35] S. Salehi, H. Nilsson, OpenFOAM for francis turbine transients, *OpenFOAM® Journal* 1 (2021) 47–61, <https://doi.org/10.7910/DVN/31JGOM>, <https://journal.openfoam.com/index.php/ofj/article/view/26>.
- [36] F. Pellegrini, J. Roman, Scotch: a software package for static mapping by dual recursive bipartitioning of process and architecture graphs, in: H. Liddell, A. Colbrook, B. Hertzberger, P. Sloot (Eds.), *High-Performance Computing and Networking*, Springer Berlin Heidelberg, Berlin, Heidelberg, 1996, pp. 493–498, https://doi.org/10.1007/3-540-61142-8_588.
- [37] A. Savitzky, M.J.E. Golay, Smoothing and differentiation of data by simplified least squares procedures, *Anal. Chem.* 36 (8) (1964) 1627–1639, <https://doi.org/10.1021/60013a027>.

- doi.org/10.1021/ac60214a047.
- [38] T. Jacob, J.-E. Prénat, Francis turbine surge: discussion and data base, in: E. Cabrera, V. Espert, F. Martínez (Eds.), *Hydraulic Machinery and Cavitation*, Springer Netherlands, Dordrecht, 1996, pp. 855–864, https://doi.org/10.1007/978-94-010-9385-9_87.
- [39] A.I. Bosioc, R. Susan-Resiga, S. Muntean, C. Tanasa, Unsteady pressure analysis of a swirling flow with vortex rope and axial water injection in a discharge cone, *J. Fluid Eng.* 134 (8) (07 2012), 081104, <https://doi.org/10.1115/1.4007074>.
- [40] M. Nishi, T. Kubota, S. Matsunaga, Y. Senoo, Study on swirl flow and surge in an elbow type draft tube, in: *Proceedings of 10th IAHR Symposium*, Tokyo, Japan, vol. 1, 1980, pp. 557–568.
- [41] K. Amiri, B. Mulu, M. Raisee, M.J. Cervantes, Unsteady pressure measurements on the runner of a Kaplan turbine during load acceptance and load rejection, *J. Hydraul. Res.* 54 (1) (2016) 56–73, <https://doi.org/10.1080/00221686.2015.1110626>.
- [42] R. Goyal, M.J. Cervantes, B.K. Gandhi, Vortex rope formation in a high head model Francis turbine, *J. Fluid Eng.* 139 (4) (02 2017), 041102, <https://doi.org/10.1115/1.4035224>.
- [43] J. Jeong, F. Hussain, On the identification of a vortex, *J. Fluid Mech.* 285 (1995) 69–94, <https://doi.org/10.1017/S0022112095000462>.